ISSN 1674-1056
http://cpb.iphy.ac.cn
http://iopscience.iop.org/cpb
中国物理 B
Chinese Physics
中国物理 Chinese Physics B

Mid-infrared supercontinuum generation and its application on all-optical quantization with different input pulses

Yan Li(李妍), Xinzhu Sang(桑新柱)

Citation: Chin. Phys. B . 2019, 28(5): 054206. **doi:** 10.1088/1674-1056/28/5/054206
Journal homepage: http://cpb.iphy.ac.cn; http://iopscience.iop.org/cpb

What follows is a list of articles you may be interested in

Experimental and numerical investigation of mid-infrared laser in Pr^{3+}-doped chalcogenide fiber

Hua Chen(陈华), Ke-Lun Xia(夏克伦), Zi-Jun Liu(刘自军), Xun-Si Wang(王训四), Xiang-Hua Zhang(章向华), Yin-Sheng Xu(许银生), Shi-Xun Dai(戴世勋)
Chin. Phys. B . 2019, 28(2): 024209. **doi:** 10.1088/1674-1056/28/2/024209

High performance GaSb based digital-grown InGaSb/AlGaAsSb mid-infrared lasers and bars

Sheng-Wen Xie(谢圣文), Yu Zhang(张宇), Cheng-Ao Yang(杨成奥), Shu-Shan Huang(黄书山), Ye Yuan(袁野), Yi Zhang(张一), Jin-Ming Shang(尚金铭), Fu-Hui Shao(邵福会), Ying-Qiang Xu(徐应强), Hai-Qiao Ni(倪海桥), Zhi-Chuan Niu(牛智川)
Chin. Phys. B . 2019, 28(1): 014208. **doi:** 10.1088/1674-1056/28/1/014208

Room-temperature continuous-wave interband cascade laser emitting at 3.45 μm

Yi Zhang(张一), Fu-Hui Shao(邵福会), Cheng-Ao Yang(杨成奥), Sheng-Wen Xie(谢圣文), Shu-Shan Huang(黄书山), Ye Yuan(袁野), Jin-Ming Shang(尚金铭), Yu Zhang(张宇), Ying-Qiang Xu(徐应强), Hai-Qiao Ni(倪海桥), Zhi-Chuan Niu(牛智川)
Chin. Phys. B . 2018, 27(12): 124207. **doi:** 10.1088/1674-1056/27/12/124207

Double-rod metasurface for mid-infrared polarization conversion

Yang Pu(蒲洋), Yi Luo(罗意), Lu Liu(刘路), De He(何德), Hongyan Xu(徐洪艳), Hongwei Jing(景洪伟), Yadong Jiang(蒋亚东), Zhijun Liu(刘志军)
Chin. Phys. B . 2018, 27(2): 024202. **doi:** 10.1088/1674-1056/27/2/024202

Self-compression of 1.8-μm pulses in gas-filled hollow-core fibers

Rui-Rui Zhao(赵睿睿), Ding Wang(王丁), Yu Zhao(赵钰), Yu-Xin Leng(冷雨欣), Ru-Xin Li(李儒新)
Chin. Phys. B . 2017, 26(10): 104206. **doi:** 10.1088/1674-1056/26/10/104206

Mid-infrared supercontinuum generation and its application on all-optical quantization with different input pulses*

Yan Li(李妍)† and Xinzhu Sang(桑新柱)

State Key Laboratory of Information Photonics and Optical Communications, Beijing University of Posts and Telecommunications, Beijing 100876, *China*

(Received 5 December 2018; revised manuscript received 17 February 2019; published online 22 April 2019)

Supercontinuum generation (SCG) and its application on all-optical quantization of all-optical analog-to-digital conversions (AOADCs) at the mid-infrared region in an AlGaAs strip waveguide are investigated numerically. The simulation results show that when the parabolic pulse is input, not only broader and higher-coherence SCG is obtained and a higher effective number of bits (ENOB) can be achieved, compared with the input pulse with hyperbolic-secant and Gaussian shaping. A four-bit quantization resolution is achieved along with a signal-to-noise ratio of 24.02 dB and an ENOB of 3.99 bit, and the required input peak power is 760 mW.

Keywords: mid-infrared, supercontinuum generation, all-optical quantization

PACS: 42.65.–k, 42.65.wi, 78.55.Cr **DOI:** 10.1088/1674-1056/28/5/054206

1. Introduction

The mid-infrared region is a very important electromagnetic radiation band containing two relatively transparent windows in the atmosphere. It covers the characteristic spectral lines of many important molecules. Therefore, a light source operating in this band is very suitable for long-distance transmission in the atmosphere, as well as for gas sensing, free space communication, and high-precision medical and military applications.[1,2] Therefore, this region has attracted considerable interest from researchers.

Supercontinuum generation refers to the fact that many new frequencies are generated in the spectrum of the transmitted pulse when a high-power ultrashort optical pulse passes through a nonlinear optical medium, such as a solid, liquid, gas, or semiconductor, owing to various nonlinear effects in the medium. Consequently, the output pulse spectral width is considerably broader than the incident pulse width. SCG relies on the interplay of nonlinear effects, such as self-phase modulation (SPM) and four-wave mixing (FWM), and most SCG studies realized with optical fibers are difficult to integrate.[3–7] Many smart SCG schemes based on various optical waveguides covering the visible and near-infrared wavelength regions were reported by many research groups over the years.[8,9] In the mid-infrared wavelength region, SCG has attracted increasing research interest.[5,10,11]

Compared with silicon-based materials and chalcogenide materials, in the mid-infrared region, GaAs with a large nonlinear refractive index and a wide transparency spectral range of 20 μm has been widely used as a substrate material.[12,13] Therefore, it is very suitable for the generating the nonlinear effect in all-optical signal processing devices. AlGaAs is an alloy of GaAs and AlAs. When the Al content in AlGaAs changes, the refractive index of AlGaAs changes.[14–16] After years of development, the preparation technology of AlGaAs has matured, which results in easy mass production and cost reduction. Thus far, the application of AlGaAs waveguides in nonlinear optics has been extensively investigated.[14–16]

Many practical applications related to all-optical signal processing, ultra-high-speed optical systems, and nonlinear optics require a large variety of pulse waveforms other than Gaussian or secant pulse waveforms. The characteristics of input pulses, such as the pulse width, pulse energy, initial chirping, and initial pulse shape are very critical from the viewpoint of pulse evolution. In recent years, rectangular and parabolic pulses have attracted considerable attention owing to their favorable properties and features, such as resistance to optical wave breaking, self-similarity in shape, and enhanced linearity in chirp.[17–19] Parabolic pulses propagate self-similarly in a dispersive medium with normal dispersion and nonlinearity. Therefore, the amplitude and width scaling depends only on amplifier parameters and the input pulse energy.[20] Owing to such features, parabolic pulses find a wide range of applications, such as pulse compression and flat spectral broadening.[21–23] Recently, many simple approaches to the generation of parabolic pulses have been demonstrated using super-structured fiber Bragg grating technology,[22,24] dispersion-decreasing fibers with normal group-velocity dispersion,[17,21,23,25] or AWG.[26]

The AOADC, which aims to overcome the drawbacks of electrical ADC, has attracted considerable attention.[27–31] As the key process of AOADC, many smart schemes of all-optical quantization techniques determining the speed and res-

*Project supported by the National Natural Science Foundation of China (Grant Nos. 61307109 and 61475023).

†Corresponding author. E-mail: liyanllyy@126.com

© 2019 Chinese Physical Society and IOP Publishing Ltd

olution of conversion were proposed with nonlinear optical effects in optical fibers,[28–36] while the vast majority of mature schemes pertaining to optical quantization employ soliton self-frequency shift (SSFS).[32–36] SCG in nonlinear media is an intensity-to-wavelength conversion of the input pulse,[37–40] and it is feasible for application in all-optical quantization. Several SCG-based quantization schemes were demonstrated by many research groups.[38–40]

Here, simulations of SCG in the mid-infrared region and its application on all-optical quantization are studied for the first time based on an AlGaAs horizontal strip waveguide with different types of input pulses, such as parabolic pulse, hyperbolic-secant pulse and the Gaussian pulse. Owing to the large nonlinear refractive index of AlGaAs, a strong nonlinear interaction is realized, and the required power consumption of the quantization scheme is reduced efficiently. Compared with the hyperbolic-secant pulse and the Gaussian pulse, the parabolic pulse offers advantages in terms of broadening, SCG coherence, and ADC performance. As a result, four-bit quantization resolution along with ENOB of 3.99 bit and a signal-to-noise ratio (SNR) of 24.02 dB are achieved with the parabolic pulse, 3.97 bit and 23.45 dB with the hyperbolic-secant pulse, 3.973 bit and 23.92 dB with the Gaussian pulse.

2. Theoretical model and waveguide design

2.1. Theoretical model

At room temperature, the Sellmeier equations of $Al_xGa_{1-x}As$ can be approximated as follows:[3,15]

$$n^2(\lambda) = A + \frac{B}{\lambda^2 - C} - D\lambda^2, \tag{1}$$

where λ is the wavelength in micrometers, and the coefficients A, B, C, D are defined as follows:

$$\begin{cases} A(x) = 10.906 - 2.92x, \\ B = 0.97501, \\ C(x) = \begin{cases} (0.52886 - 0.735x)^2, & 0 \leqslant x \leqslant 0.36, \\ (0.30386 - 0.105x)^2, & 0.36 < x \leqslant 1, \end{cases} \\ D(x) = 0.002467(1.41x + 1), \end{cases} \tag{2}$$

where, x represents the molar content of aluminum in AlGaAs.

The dynamic process of pulse propagation in the AlGaAs waveguide can be modeled with the generalized nonlinear Schrödinger equation (GNLSE)[41] (Eq. (3)) and solved with the fourth-order Runge–Kutta formula

$$\frac{\partial A(z,t)}{\partial z} + \frac{\alpha}{2}A(z,t) - \sum_{m\geqslant 0} \frac{\mathrm{i}^{m+1}\beta_n(\omega)}{m!}\frac{\partial^m A(z,t)}{\partial t^2} = \mathrm{i}\gamma\left(1 + \frac{\mathrm{i}}{\omega_0}\frac{\partial}{\partial t}\right) \times \left(A(z,t)\int_0^{+\infty} R(t')\left|A(z,t-t')\right|^2 \mathrm{d}t'\right), \tag{3}$$

where $A(z,t)$ is the slowly varying envelope of the electric field, α is linear loss of the waveguide, and $\beta n(\omega)$ is the n-th order dispersion parameter coefficient at the center frequency ω_0. The last item on the right side of equation (3) represents third-order nonlinear effects, including self-phase modulation (SPM) and delayed Raman response.[42]

$$R(t) = (1 - f_R)\delta(t) + f_R h_R(t), \tag{4}$$

$h_{R(t)}$ as the Raman response function of the waveguide is given as follows:[42]

$$h_R(t) = \frac{\tau_1^2 + \tau_2^2}{\tau_1 \tau_2^2}\exp(-t/\tau_2)\sin(t/\tau_1). \tag{5}$$

Here, τ_1 and τ_2 are two adjustable parameters. In the normal dispersion regime, $R(t)$ is negligible owing to the small contribution of the Raman effect to SC generation. In the normal dispersion region, the main cause of SCG is SPM.

The hyperbolic-secant pulse occurs naturally in the context of optical solitons and pulses emitted from a few mode-locked lasers.[43] The temporal envelope expression associated with such pulse is often described with the following form:

$$A_P(t) = \sqrt{P_P}\,\mathrm{sech}\left(\frac{2\sqrt{\ln 2}}{T_P}t\right), \tag{6}$$

and the temporal envelope of the Gaussian pulse can be described as

$$A_P(t) = \sqrt{P_P}\exp\left(-\mathrm{i}\frac{(2\sqrt{\ln 2})^2}{2T_P^2}t^2\right). \tag{7}$$

Compared to the other pulse shapes, the parabolic pulse is maintained as the pulse undergoes exponential temporal and spectral broadening as well as an increase in amplitude. Furthermore, the parabolic pulse can resist the deleterious effects of wave breaking, which severely degrades the evolution of pulses evolving in a nonlinear dispersive medium. The analytical expression for a parabolic pulse of energy is as follows:

$$A_P(t) = \begin{cases} \sqrt{P_P}\sqrt{1 - 2\dfrac{t^2}{T_P^2}}\exp\left(-\mathrm{i}\dfrac{C_P}{2}t^2\right), & |t| \leq T_P/\sqrt{2}, \\ 0 & |t| > T_P/\sqrt{2}. \end{cases} \tag{8}$$

In the above formulas, P_P is the peak power of the pulse, T_P is the temporal full-width at half-maximum, and C_P is the linear chirp coefficient. At mid-infrared, the parabolic pulse can be generated in a tapered chalcogenide microstructured optical fiber,[44] or tapered silicon photonic wires.[45]

2.2. Waveguide design

As shown in Fig. 1(a), the waveguide is used with a strip structure. The core domain consists of $Al_{0.18}Ga_{0.82}As$, substrate domain is made of $Al_{0.8}Ga_{0.2}As$, and the upper cladding region is air. Specifically, the dispersive value of the TE mode is smaller than that of the TM mode. Hence, the quasi-TE

mode is selected as the propagation mode for this waveguide. The full-vector finite element method was used to analyze the mode field distribution. The width $w = 6$ μm and height $h = 2.5$ μm of the waveguide are optimized by analyzing the effect of the waveguide geometrical parameters on the dispersion and effective mode area for maximal nonlinear interaction. Most of the guided-mode energy is confined tightly within the core.

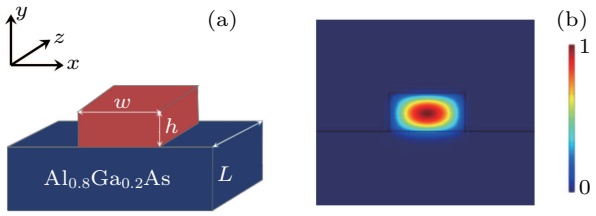


Fig. 1. (a) Designed waveguide and (b) transverse profile of electric field for quasi-TE polarization.

The nonlinear coefficient, $\gamma_0 = 2\pi n_2/\lambda_0 A_{\text{eff}}$, is determined by two factors, namely, nonlinear refractive index n_2 and effective mode area A_{eff} (Eq. (9)).

$$A_{\text{eff}} = \frac{\left(\int\int_{-\infty}^{+\infty} |F(x,y)|^2 \,\mathrm{d}x\mathrm{d}y\right)^2}{\int\int_{-\infty}^{+\infty} |F(x,y)|^4 \,\mathrm{d}x\mathrm{d}y}, \tag{9}$$

where $F(x,y)$ is the modal distribution of the fundamental waveguide mode.

The GVD is calculated as $D = -(\lambda/c)\,\mathrm{d}^2 n_{\text{eff}}/\mathrm{d}\lambda^2$, where n_{eff} is the effective refractive index of the waveguide. Figure 2 shows the GVD parameter and β_2 as a function of the wavelength. Both β_2 and D vanish at the zero-dispersion wavelength near 3.6 μm. A_{eff} of the designed waveguide at 3 μm is 0.058 μm^2, and the nonlinear coefficient is $\gamma = 180.55$ W^{-1}/m. The software COMSOL is used to calculate the effective index that yields the propagation constant β. If the number of dispersion terms is insufficient during SCG simulations, it is possible to result in inaccurate or deceptive results. Equation (3) is solved up to the 11th order of dispersion and the dispersion data are fitted with Taylor series expansion up to the 11th order of dispersion. The high-order dispersion coefficients at 3 μm are calculated, and they are listed in Table 1.

Table 1. The dispersion coefficients.

β_2	2.48×10^{-25} s^2/m	β_7	-1.12×10^{-94} s^7/m
β_3	2.12×10^{-39} s^3/m	β_8	1.01×10^{-108} s^8/m
β_4	-2.08×10^{-24} s^4/m	β_9	1.02×10^{-121} s^9/m
β_5	1.28×10^{-67} s^5/m	β_{10}	3.67×10^{-136} s^{10}/m
β_6	-2.51×10^{-81} s^6/m	β_{11}	-4.92×10^{-149} s^{11}/m

AlGaAs is a widely used semiconductor material, and its production process is rather mature. AlGaAs growth can be achieved by using molecular beam epitaxy or metal organic chemical vapor deposition with GaAs crystal as the substrate. By using dry etching or wet etching, the desired waveguide shape can be obtained and subsequently packaged.

3. Simulation and discussion

The designed III–V waveguide described above is used to generate supercontinuum in the mid-infrared region. The GNLSE given by Eq. (3) is numerically solved for SCG. The length of the waveguide $L = 1$ cm. Figure 3 shows SCG with different input powers (P_0) for the input pulse width $T_0 = 100$ fs at -20 dB level and peak power of the input pulses set to 100 mW, 1 W, 10 W, and 100 W. SCG with different input pulse widths (T_0) is shown for the input power $P_0 = 10$ W at -20 dB and pulse width set to 100 fs, 300 fs, 500 fs, and 1 ps, respectively. When the initial width of the incident pulse and the peak power are not the same, the effect of dispersion and nonlinear effects on pulse evolution are also different. The narrower the initial pulse width is, the stronger the dispersion effect is. The higher the peak power of the initial pulse, the stronger the nonlinear effect is. Whether the input pulse is hyperbolic-secant (Figs. 3(b), 3(e), 3(h), 3(k); Figs. 4(b), 4(e), 4(h), 4(k)), Gaussian (Figs. 3(c), 3(f), 3(i), 3(l); Figs. 4(c), 4(f), 4(i), 4(l)), or parabolic (Figs. 3(a), 3(d), 3(g), 3(j); Figs. 4(a), 4(d), 4(g), 4(j)), the spectral width of SCG increases as the input power increases with the same input pulse width. The input pulse width is narrower, and the spectrum of the supercontinuum is broader for the same input power. Compared with the hyperbolic-secant pulse and the Gaussian pulse, the parabolic pulse can generate a wider spectrum for the same input pulse power or pulse width. The influence of input power on the parabolic pulse is more obvious than that on the hyperbolic-secant pulse and the Gaussian pulse.

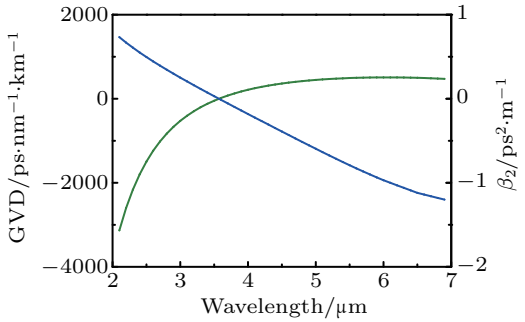


Fig. 2. Variation of β_2 and D with wavelength. Both β_2 and D vanish at the zero-dispersion wavelength near 3.6 μm.

Coherence describes the spectral randomness of SC under the influence of random amplitude and phase noise. If coherence is poor, the spectrum generated with different input pulses into the waveguide shows large random fluctuations owing to random power noise and phase noise, which means the system is sensitive to the random noise in the incoming signal when the coherence of SCG is low, and excessive randomness of the spectrum leads to inconsistency in the amount of spectral spread determined at the same power, resulting in erroneous coding. A suitable measure of coherence for SCG is the degree of coherence associated with each spectral component. First-order coherence is defined as follows:[42,43]

$$\left|g_{12}^{(1)}(\lambda)\right| = \left|\frac{\left\langle \tilde{A}_1^*(\lambda)\tilde{A}_2(\lambda)\right\rangle}{\sqrt{\left\langle\left|\tilde{A}_1(\lambda)\right|^2\right\rangle\left\langle\left|\tilde{A}_2(\lambda)\right|^2\right\rangle}}\right|, \tag{10}$$

where $\tilde{A}(\lambda)$ is the amplitude of the SC generated in the frequency domain. To obtain more accurate results, 100 pairs with independent random power noise and phase noise are used in the simulation.

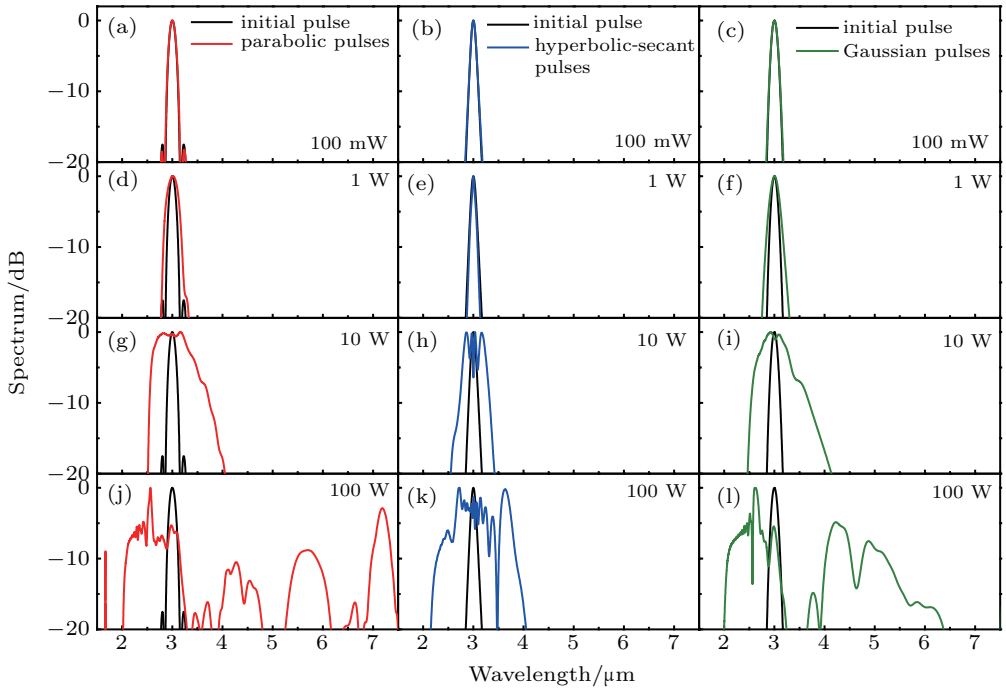


Fig. 3. Spectra obtained with different pumping powers ($T_0 = 100$ fs). The input pulses of panels (a), (d), (g), and (j) are parabolic pulses. The input pulses of panels (b),(e), (h), and (k) are hyperbolic-secant pulses. The input pulses of panels (c), (f), (i), and (l) are Gaussian pulses. $L = 1.5$ cm.

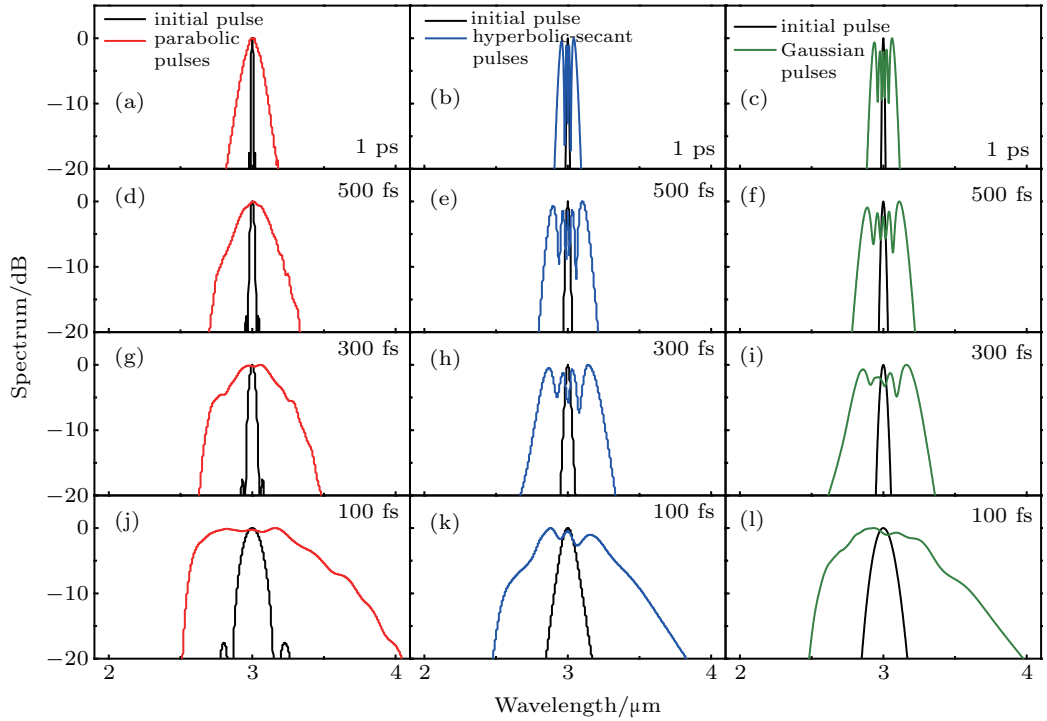


Fig. 4. Spectra obtained with different pumping widths ($P_0 = 10$ W). The input pulses of panels (a), (d), (g), and (h) are parabolic pulses. The input pulses of panels (b), (e), (h), and (k) are hyperbolic-secant pulses. The input pulses of panels (c), (f), (i), and (l) are Gaussian pulses. $L = 1.5$ cm.

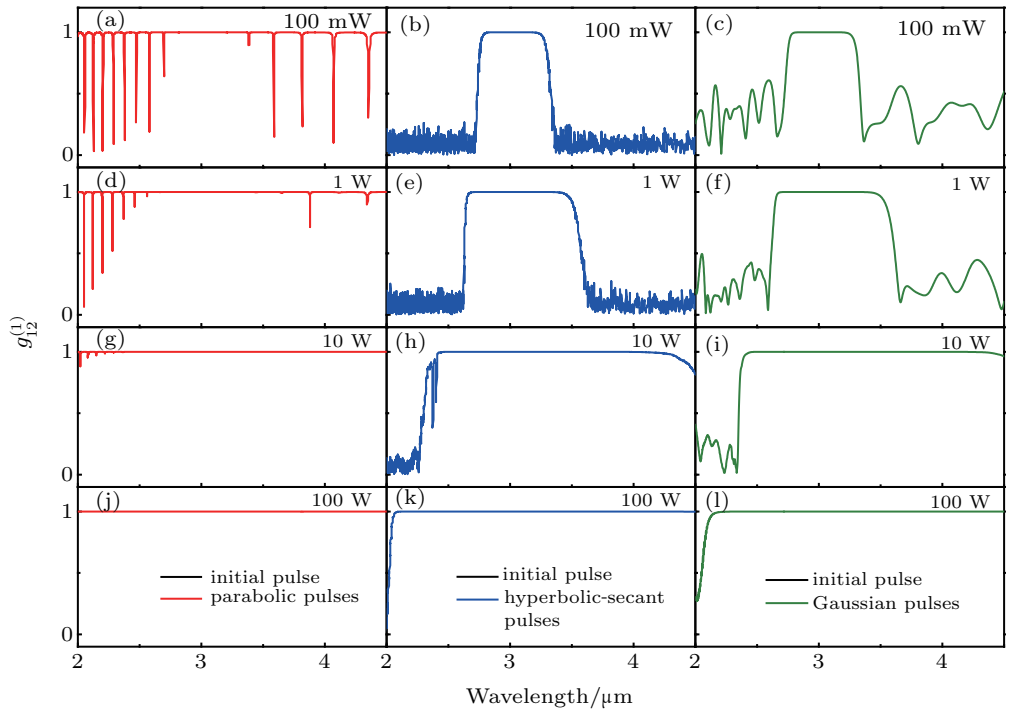


Fig. 5. Degrees of coherence. The input pulses of panels (a), (d), (g), and (j) are parabolic pulses. The input pulses of panels (b), (e), (h), and (k) are hyperbolic-secant pulses. The input pulses of panels (c), (f), (i), and (l) are Gaussian pulses, when $T_0 = 100$ fs.

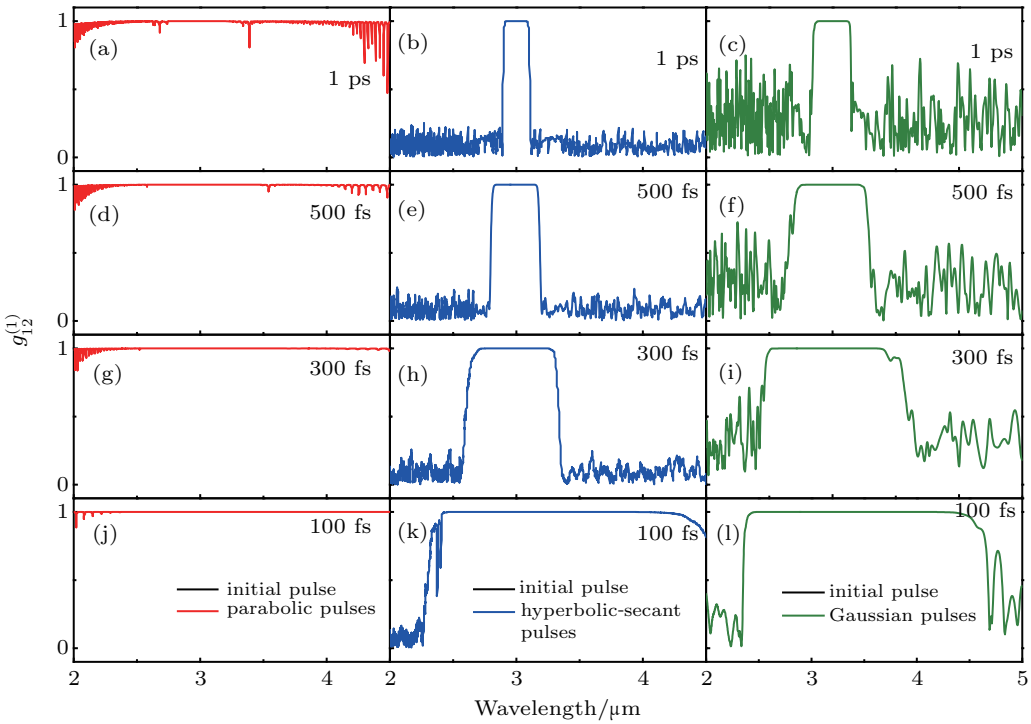


Fig. 6. Degrees of coherence. The input pulses of panels (a), (d), (g), and (j) are parabolic pulses. The input pulses of panels (b), (e), (h), and (k) are hyperbolic-secant pulses. The input pulses of panels (c), (f), (i), and (l) are Gaussian pulses, when $P_0 = 10$ W.

The degrees of coherence corresponding to Figs. 3 and 4 are shown in Figs. 5 and 6, respectively. Both degrees of coherence around 3 μm are almost 1. The coherence of the parabolic pulse is better than that of the hyperbolic-secant pulse and the Gaussian pulse under the same conditions. Excellent coherence can ensure stability of the quantization scheme. On the contrary, a coding error can occur when the degree of coherence is not 1. Thus, it is essential that the degree of coherence be close to 1 in quantization schemes that employ slicing SC.

The schematic diagram of the proposed quantization scheme by slicing SC is shown in Fig. 7. The sampled pulses with different peak powers are incident on the designed III–V waveguide. To indicate variations of the different pulses,

two pulses with different peak powers and the same central wavelength λ_0 are plotted. Spectrum broadening of the optical pulses occurs due to the interaction between waveguide dispersion and nonlinearity. Therefore, the intensity of the sampled pulse can be converted into the SC width of the optical parameters. By measuring the width of the SC, the input sampled pulse can be quantized. To determine the width of the generated SC, a set of filters can be placed in the long-wave direction at the input pulse center wavelength. At the output end of each filter, the optical signals are converted into electrical signals by photodetectors, and these electrical signals are judged using comparators.[46,47] A decision threshold is set. If the detector output exceeds the fixed threshold, the state of the port is "ON", and the marked code is "1". Otherwise, the state of port is "OFF", and the code is "0".

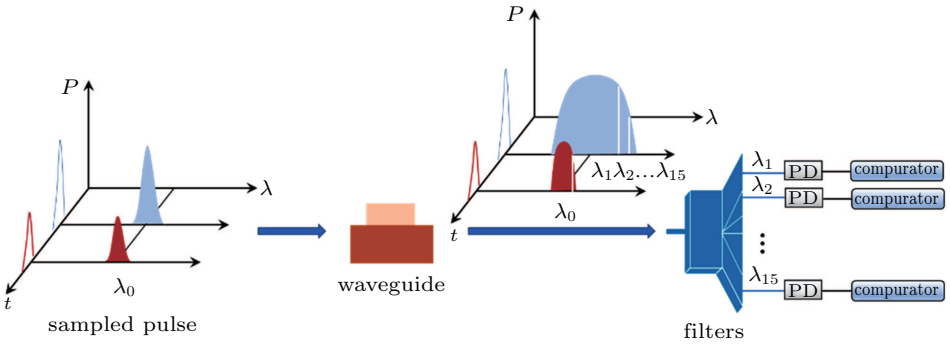


Fig. 7. Schematic diagram of proposed spectral quantization (PD: photoelectric detector).

For this scheme, the width of the input pulse with a center wavelength of 3 μm is set to 100 fs. The input pulse power is increased from 200 mW to 760 mW. The −15 dB band- width of SCG is measured, as shown in Fig. 8. Fifteen filters are used to slice the generated SC to achieve four-bit quantization resolution. A nonlinear relationship exists between the peak power of the input pulse and the width of the SC, and special design of the non-uniform filters can improve the system resolution. Tables 1, 2, and 3 list the center wavelengths of the filters. The research on mid-infrared tunable filters is becoming increasingly mature,[48–51] and tunable filters with AlGaAs waveguides was studied, which can be used for integration.[49]

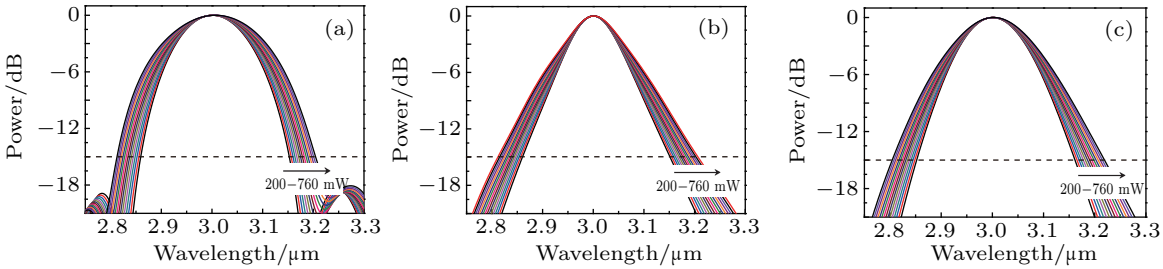


Fig. 8. Spectrum width for different input peak powers: (a) parabolic pulse, (b) hyperbolic-secant pulse, and (c) Gaussian pulse.

Table 2. The center wavelength of the 15 filters for the hyperbolic-secant pulse.

No.	Center wavelength/nm	No.	Center wavelength/nm	No.	Center wavelength/nm
1	3151	6	3170	11	3188
2	3155	7	3174	12	3192
3	3159	8	3177.5	13	3195.5
4	3163	9	3181	14	3199
5	3166.6	10	3184.5	15	3203

Table 3. The center wavelength of the 15 filters for the parabolic pulse.

No.	Center wavelength/nm	No.	Center wavelength/nm	No.	Center wavelength/nm
1	3152.5	6	3171	11	3189.5
2	3156	7	3174.5	12	3193
3	3160	8	3178.5	13	3197
4	3163.5	9	3182	14	3201
5	3167	10	3185.5	15	3204.5

Table 4. The center wavelength of the 15 filters for the Gaussian pulse.

No.	Center wavelength/nm	No.	Center wavelength/nm	No.	Center wavelength/nm
1	3151.8	6	3170.2	11	3188.5
2	3155.8	7	3174.2	12	3192.5
3	3159.2	8	3178	13	3195.6
4	3163.2	9	3181.5	14	3199.8
5	3166.8	10	3185	15	3204

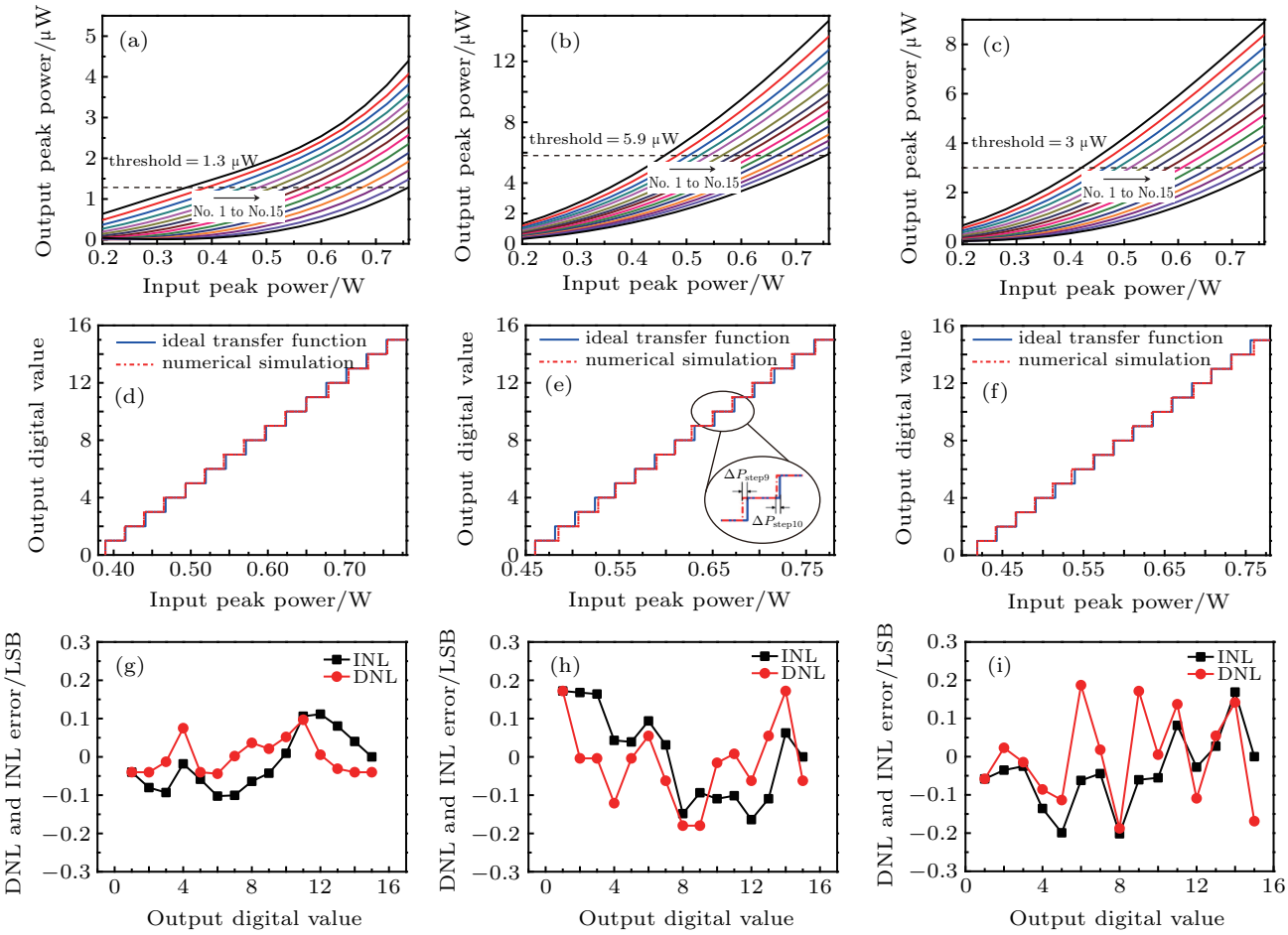


Fig. 9. Output peak powers of 15 filtering ports spaced evenly as a function of input peak powers ((a), (b), (c)). The corresponding quantization transfer function of the four-bit quantization scheme ((d), (e), (f)). Differential nonlinear error and integral nonlinear error with the filtering ports ((g), (h), (i)). The input pulses of panels (a), (d), and (h) are parabolic pulses. The input pulses of panels (b), (e), and (h) are hyperbolic-secant pulses. The input pulses of panels (c), (f), and (i) are Gaussian pulses.

On the Stokes side of the pump wavelength, the change in filter power from mark "0" to "1" to the next filter from "0" to "1" corresponds to the least significant bit (LSB) of the designed filter. Nos. 1 to 15 in Fig. 9(a), 9(b), and 9(c) represent the first to the fifteenth filters. When the input pulse is hyperbolic-secant, 3151 nm–3203 nm range is selected as the filtering area, and 5.9 μW is used as the power threshold. From Fig. 9(b), it can be seen that the power used for quantification is 460 mW–760 mW, and the LSB is 20 mW. The corresponding transfer function is shown in Fig. 9(e), where the solid line (blue) represents the ideal transfer function, and the dashed line (red) represents the simulated transfer function. When the input pulse is Gaussian, we set 3151 nm–3203 nm as the filtering range and 3 μW as the power threshold. From Fig. 9(b), the power used for quantification is 410 mW–760 mW, and the LSB is 23.3 mW. The corresponding transfer function is shown in Fig. 9(e). When the input pulse is parabolic, we set 3314 nm–3374 nm as the filtering area and 1.9 μW as the power threshold. From Fig. 9(a), the power used for quantification is 360 mW–760 mW, and the LSB is 26.7 mW. The larger LSB is beneficial for improving ENOB. The corresponding transfer function is shown in Fig. 9(d). It can be seen from Figs. 9(d)), 9(e), and 9(f) that difference exists between the simulated and the ideal values. The calculated differential nonlinear error (DNL) and the integral nonlinear error (INL) errors[50] are shown in Figs. 9(g), 9(h), and 9(i). The maximum value of DNL is 0.18 LSB and that of INL is 0.17 LSB when the input pulse is hyperbolic-secant. The maximum value of DNL is 0.17 LSB and that of INL is 0.15 LSB when the input pulse is Gaussian. The maximum value

of DNL is 0.09 LSB and that of INL is 0.11 LSB when the input pulse is parabolic. The effective number of bits (ENOB) and the signal-to-noise ratio (SNR) were found to be 3.97 bit and 23.54 dB for the hyperbolic-secant pulse, 3.973 bit and 23.92 dB for the Gaussian pulse, and 3.99 bit and 24.02 dB for the parabolic pulse.

With increased spectral bandwidth, this scheme can be used to achieve high speed and multi-bit quantization. As seen from Fig. 10, when NOB = 2, 3, 4, the corresponding ENOB of parabolic pulse is higher than that of gaussian pulse and hyperbolic secant pulse, but the difference is not large. When NOB = 5, 6, the difference between the ENOB corresponding to the parabolic pulse and the ENOB of the Gaussian pulse and the hyperbolic secant pulse is high up to 0.5 bit. Therefore, it can be seen from the Fig. 10, compared with gaussian pulse and hyperbolic secant pulse, the parabolic pulse shows noticeable improvement of ENOB. The advantages of the parabolic pulse are more obvious at higher resolutions.

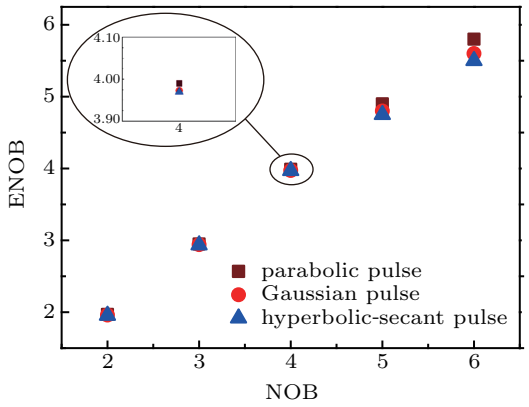


Fig. 10. Relationship between NOB and ENOB for different pulses.

4. Conclusion

In summary, the influences of pulse width, peak power, and pulse type on SCG with an AlGaAs horizontal strip waveguide is investigated in the mid-infrared region, their effects on all-optical quantization of AOADC are also dicussed with different input pulses. Results show that when the type of input pulse is parabolic, the SCG is broader and has higher coherence. Owing to the high nonlinear coefficient of the III–V waveguide in the mid-infrared region in this scheme, the input pulse peak power required to reach the appropriate SCG is reduced, resulting in low power consumption and an integrated quantization scheme. The generated high-coherence SC can be used for AOADC applications to reduce coding error and enhance ENOB. The SNR and ENOB are 23.54 dB and 3.97-bit for the hyperbolic-secant pulse, 23.92 dB and 3.973-bit for the Gaussian pulse, and 24.02 dB and 3.99-bit for the parabolic pulse. In an M-bit ($M > 4$) quantization scheme, the advantages of the parabolic pulse will be more obvious.

References

[1] Dai S X, Chen H G, Li M Z, Jiang J, Xu T F and Nie Q H J 2012 *Infrared Laser Eng.* **41** 4847 (in Chinese) ISSN: 1007-2276
[2] Jonathan H, Price H V, Monro T M, Feng X and Richardson D J J 2007 *J. Sel. Top. Quantum. Electron.* **13** 738
[3] Agrawal G P 2013 *Nonlinear Fiber Opt.* 5th edn., p. 388
[4] Li X, Chen W, Xue T F and Liao M S J 2014 *Opt. Express* **22** 24179
[5] Han Y, Hou L T and Zhou G Y J 2012 *Chin. Phys. Lett.* **29** 54208
[6] Hu H Y, Li W B and Dutta N K J 2013 *Appl. Opt.* **52** 7336
[7] Swiderski J and Maria M J 2014 *Opt. Lett.* **39** 910
[8] Fedotova O A and Herrmann J J 2006 *Opt. Express* **14** 1512
[9] Xiang B X, W L and Ma Y J J 2017 *Chin. Phys. Lett.* **34** 38
[10] Yu Y, Wang T, Ma P and Barry D V J 2013 *Opt. Mater. Express* **3** 1075
[11] Karim M R, Rahman B M A and Agrawal G P J 2015 *Opt. Express* **23** 6903
[12] Adachi S J 1985 *J. Appl. Phys.* **58** R1
[13] Zhang L J 2014 *Nanophotonics* **3** 247
[14] Siviloglou G A, Suntsov S and Sorel M J 2006 *Opt. Express* **14** 9377
[15] Jang P K and Sarangan A M J 2007 *Opt. Lett.* **32** 536
[16] Wang G H and Zhang J K J 2018 *Chin. Phys. B* **27** 027801
[17] Toshihiko Hirooka and Masataka Nakazawa J 2004 *Opt. Lett.* **29** 498
[18] Wabnitz S, Finot C and Sysoliatin A 2007 *CLEO*, May 6–11, 2007, Baltimore, USA, p. CThQ3
[19] Finot C, Dudley J M and Kibler B J 2006 *IEEE J. Sel. Top. Quantum Electron.* **45** 1482
[20] Huh J and Azaña J 2015 *CLEO: Sci. Innovat.* May 10–15, 2015, San Jose, USA, p. SM2P.6
[21] Kwon Y, Vazquez-Zuniga L A and Hong S 2013 *Conference on Lasers and Electro-Optics/Pacific Rim* June 30–July 4, 2013, Kyoto, Japan, p. WPB_20
[22] Finot C, Richardson D J and Parmigiani F J 2006 *Opt. Express* **14** 7617
[23] Shulika O V, Sukhoivanov I A and Ramosortiz G J 2014 *Nanophotonics* **8** 083890
[24] Parmigiani F, Petropoulos P, Ibsen M and Richardson D J J 2006 *IEEE Photon. Technol. Lett.* **18** 829
[25] Sukhoivanov I A, Iakushev S O and Shulika O V J 2013 *Opt. Express* **21** 17769
[26] Okamoto K, Nakazawa M and Hirooka T J 2008 *Opt. Lett.* **33** 1102
[27] Valley G C J 2007 *Opt. Express* **15** 1955
[28] Ikeda K, Abdul J M and Shu N J 2005 *Opt. Express* **13** 4296
[29] Satoh T, Itoh K and Konishi T J 2013 *IEICE Trans. Electron.* **96** 223
[30] Takahashi K, Matsui H and Nagashima T J 2013 *Opt. Lett.* **38** 4864
[31] Konishi T, Tanimura K and Asano K J 2002 *J. Opt. Soc. Am. B* **19** 2817
[32] Oda S, Maruta A and Kitayama K J 2004 *IEEE Photon. Technol. Lett.* **16** 2587
[33] Kang Z, Yuan J H, Li S and Yu C X J 2013 *Chin. Phys. B* **22** 114211
[34] Xiao P, Chen Y, Wu K, Chen J and Chen X 2014 *Asia Communications and Photonics Conference*, November 11–14, 2014, Shanghai, China, p. AF3C. 3
[35] Kang X, Yuan J H, Kang Z, Yu C X J 2015 *Opt. Commun.* **355** 479
[36] Maruta A and Oda S J 2008 *Opt. Photon. News* **19** 30
[37] Oda S I and Maruta A 2005 *IEEE Photon. Technol. Lett.* **17** 465
[38] Oda S I and Maruta A 2005 *Optical Fiber Communication Conference*, March 6, 2005, Anaheim, USA, p. OThN3
[39] Kang S, Yuan J H and Kang Z J 2015 *J. Opt.* **17** 085502
[40] J T Boyd J 1972 *IEEE J. Sel. Top. Quantum Electron.* **8** 788
[41] Li F, Li Q, Yuan J H and Wai P K A J 2014 *Opt. Express* **22** 27339
[42] Genty G, Surakka M and Turunen J J 2011 *J. Opt. Soc. Am. B* **28** 1
[43] Yu K C S, Fehrembach A L and Lemarchand F 2011 *Lasers & Electro-optics Europe*, May 22–26, 2011, Munich, Germany, p. CK_P7
[44] Barh A, Ghosh S and Varshney R K J 2014 *IEEE J. Sel. Top. Quantum Electron.* **20** 590
[45] Lavdas S, Driscoll J B and Jiang H J 2013 *Opt. Lett.* **38** 3953
[46] Li P, Yi X and Liu X J 2016 *Sci. Rep.* **6** 31903
[47] Li P, Sang L and Zhao D J 2017 *J. Lightwave Technol.* **35** 5034
[48] Hawkins G, Sherwood R and Djotni K 2008 *Proceedings of SPIE — The International Society for Optical Engineering*, September 25, 2008, p. 710114
[49] Derelle S, Pardo F and Primot J 2012 *SPIE* **8424** 45
[50] Tilden S J, Linnenbrink T E and Green P J S 1999 1999 *IMTC/99 Proc. of the 16th Instrumentation and Technology Conf.* **3**
[51] Asgari S, Rajabloo H and Granpayeh N J 2018 *Chin. Phys. B* **27** 084212